Superstructure manipulation on a clean Ge(001) surface by carrier injection using an STM

Y. Takagi,* K. Nakatsuji, Y. Yoshimoto, and F. Komori[†]

Institute for Solid State Physics, University of Tokyo, Kashiwanoha 5-1-5, Kashiwashi, Chiba 277-8581, Japan
(Received 1 August 2006; revised manuscript received 31 October 2006; published 7 March 2007)

A topological defect, which is formed at the boundary between the two stable superstructures on the clean Ge(001) surface, $c(4\times2)$ and $p(2\times2)$, can be laterally manipulated at 80 K by injection of carriers into the surface states from a metal tip of the scanning tunneling microscope (STM). We measured the probability of the defect motion as functions of the direction from the defect to the injection point, the distance between them, and the bias voltage during the carrier injection. Observed anisotropy of the probability on the lateral directions is attributed to the anisotropic propagation of the carriers in the surface electron and hole bands. For the electron propagation, the probability at the fixed distance in the directions both parallel and perpendicular to the Ge dimer axis is larger on the $p(2\times2)$ surface than on the $c(4\times2)$ surface. The observed decay of the standing waves of the surface π^* electrons indicates that the difference is caused by the energy relaxation of electrons due to inelastic scattering. The most stable position of the defect depends on the sample bias voltage during the carrier injection. This suggests that the electric field due to the STM tip mainly determines the direction of the defect motion.

I. INTRODUCTION

Local carrier injection into atoms or molecules at the solid surface sometimes induces dynamical processes of the surface atoms. Desorption of atoms[1] and dissociation and rotation of molecules[2,3] have been reported on both semiconductor and metal surfaces by injecting electrons or holes from a metal tip using scanning tunneling microscope (STM).[4] Recently, the authors have reversibly manipulated the buckling orientation of dimers on the Ge(001) clean surface by carrier injection using STM.[5,6] These dynamical processes are attributed to electronic excitation of the local vibration between atoms at surfaces.[7]

The Ge(001) clean surface consists of buckled dimers, and its buckling orientation alternates in the direction perpendicular to the dimer axis (the dimer-row direction). Two arrangements of the buckled dimers are known to be stable on the surface. One is the $c(4\times2)$ structure and the other is $p(2\times2)$, as schematically illustrated in Figs. 1(a) and 1(b). The energy difference between the two superstructures, $c(4\times2)$ and $p(2\times2)$, is estimated to be a few meV/dimer according to first-principles calculations.[8] We can transform one structure into the other with hysteresis by changing the sample bias voltage V_b during STM observations below 80 K,[5,9] as in Fig. 1(c). A topological defect at the boundary between the two superstructures, that is, a pair of the adjacent Ge dimers in the dimer-row direction with the same buckling orientation, plays an important role in these structure transformations. There are two types of the topological defect, in $c(4\times2)$ and in $p(2\times2)$, and their models and STM images are shown in Figs. 1(d) and 1(e). Hereafter, we call the defect a "kink" for simplicity, and those shown in Figs. 1(d) and 1(e) are A-type and B-type kinks, respectively. In an A-type kink, the surface structure is $c(4\times2)$ except on one side of the kink in the dimer-row directions, while in a B-type kink, it is $p(2\times2)$ except on one side of the kink in the dimer-row direction.

A pair of kinks is created in the dimer row under the STM tip by a single electron process due to carrier injection into

the surface from the STM tip.[5] For example, A-type kinks were made by changing V_b from −0.4 to 0.8 V for a few seconds by fixing the tip position over a dimer in the $c(4\times2)$ surface. Then, a one-dimensional area of the $p(2\times2)$ structure appears under the STM tip with A-type kinks at both ends of the area. In the electron injection case, the threshold bias voltage for the creation of the kink pairs is 0.8 V. In the case of hole injection by changing V_b to a negative value below −0.7 V on the $p(2\times2)$ surface, a two-dimensional area of the $c(4\times2)$ structure appears. Here, B-type kinks are created both in the dimer row, where holes are injected, and in the several dimer rows neighboring it. A single B-type kink shown in Fig. 1(e) can be prepared by erasing the extra $c(4\times2)$ area by additional electron injection. The threshold bias voltage for the kink creation is −0.7 V. These threshold values determine the threshold bias voltage for the structure transformations shown in Fig. 1(c).

The carrier injection also induces kink motion in the dimer-row direction nonlocally. The kink moves when the carrier is injected into the dimer row including the kink or even into the dimer rows neighboring that dimer row. The direction of the kink motion is not fixed, but the kink tends to move toward a preferred point on the dimer row. By repeating the carrier injection, the kink comes close to the preferred point and then moves randomly around it. The distance between the preferred point and the carrier-injection point depends on V_b during carrier injection. The distance is much longer in the dimer-row direction than in the dimer-axis direction for electron injection, while the anisotropy of the distance is small for hole injection. On the basis of these experimental results, a carrier propagation model for kink motion by carrier injection was proposed.[6] The threshold bias voltage for kink motion is 0.6 V for electron injection. This is 0.2 V smaller than that of kink creation. On the other hand, for hole injection, it is −0.7 V and is the same as that of kink creation. The surface structures can be clearly imaged without moving the kink using V_b=−0.4 V and I_t =1 nA, for example.
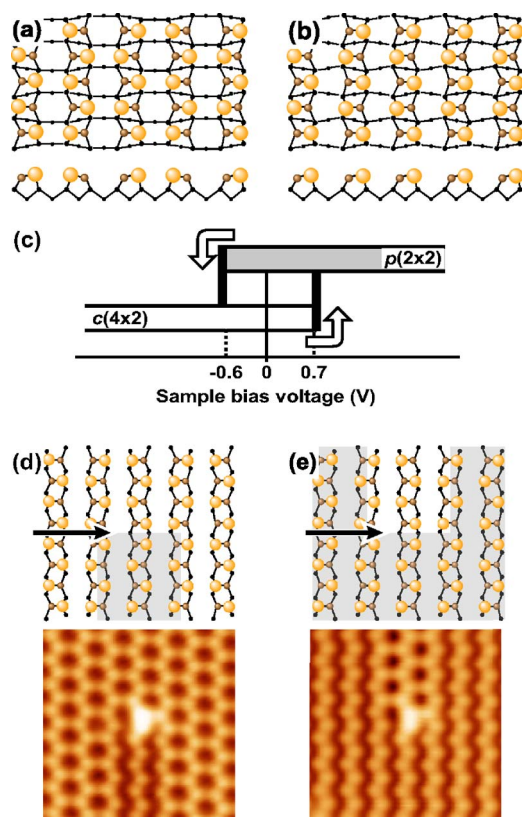
FIG. 1. (Color online) [(a) and (b)] Schematic illustrations of two stable superstructures on the Ge(001) surface; (a) $c(4\times2)$ and (b) $p(2\times2)$. Each upper panel is the top view, and the lower the side view. (c) Superstructures appearing as functions of the sample bias voltage V_b during STM observations at 80 K. Both superstructures are stable between $V_b=-0.5$ and +0.5 V and appear depending on the direction of the V_b change. The arrows indicate the directions of the bias change. [(d) and (e)] Schematic models and STM images of the two types of topological defects, (d) A-type and (e) B type, between the two superstructures. They were created on the $c(4\times2)$ surface (A) or on the $p(2\times2)$ surface (B). The $p(2\times2)$ area is shaded on the illustrations.

The creation and the movement of the kink by carrier injection are the elementary processes for the structure transformation shown in Fig. 1(c). By scanning the surface with the STM tip, kink pairs and, thus, the small area of $p(2\times2)$ in the $c(4\times2)$ surface for a positive sample bias or that of $c(4\times2)$ in $p(2\times2)$ for a negative sample bias are created under the tip. Then, the area further expands by the movement of the kinks during scanning of the tip. The threshold bias voltage of the kink creation determines that of the structure transformation.

The electronic structure of the clean Ge(001) surface is crucial for the discussion of carrier injection and carrier propagation in the surface states. The occupied states of Ge(001) have been investigated by angle-resolved photo-emission spectroscopy (ARUPS).[10–12] However, there was a controversy concerning whether the valence band top at the $\bar{\Gamma}$ point is the bulk state or the surface state. Quite recently, both occupied and unoccupied electronic states were studied using ARUPS, standing-wave observations by STM, and the

calculation of the band structure for the $c(4\times2)$ surface.[13] The observed results have removed the controversy on the valence electronic states, and the quasi-one-dimensional unoccupied surface π^* band is clearly confirmed. Moreover, they are consistent with the calculated electronic structure. Now, we can use these results to discuss the detailed processes of kink formation and kink movement induced by carrier injection from the STM tip.

The structural changes of the clean Si(001) surface, which consists of buckled dimers as for the clean Ge(001) surface, have been reported below 40 K.[14] The 2×1 local structures on the Si(001) surface observed by STM below 10 K (Refs. 15 and 16) have been recently ascribed to the motion of kinks, similar to those on Ge(001).[17] In addition, the surface superstructure of Si(001) transforms between $c(4\times2)$ and $p(2\times2)$ by scanning the surface with the STM tip,[18–20] as on the Ge(001) surface. Thus, the mechanism of the structural changes is common in these two surfaces.

In the present paper, we will show detailed results of kink motions by carrier injection into the Ge(001) surface states and will discuss them using recent knowledge of the surface electronic structure. We studied the motion as functions of the directions and the distance between the kink and the injection point. The characteristic distance for kink motion depends on the direction, the surface superstructure, and the sample bias voltage during injection. For further discussion on the difference of the carrier propagation between $c(4\times2)$ and $p(2\times2)$, we measured the decay of the standing waves in the π^* band on both surfaces. We also calculated the kink electronic state using the first-principles method to discuss the preferred direction of the kink motion. The observed results on the kink motion are consistent with the proposed model based on carrier propagation and its energy relaxation in the surface states.

II. METHODS

Experiments were done in an ultrahigh-vacuum (UHV) system, with a base pressure of below 1×10^{-8} Pa, consisting of two UHV chambers, a preparation chamber, and an STM chamber.[21] Germanium specimens were cut to the size of $8\times3\times0.4$ mm^3 from an n-type (Sb doped, 0.35 Ω cm at room temperature) Ge(001) wafer. The Ge(001) clean surface was prepared by several repetitions of Ar-ion bombardment (1 keV, 2.5 μA cm^{-2}, 10 min) and annealing at 1000 K for 10 min by passing dc directly through the specimen in the preparation chamber. We made a large area of the $p(2\times2)$ structure by scanning the surface at $V_b=1.2$ V and a tunneling current I_t of 1 nA (Refs. 5 and 9), typically. We can convert the $p(2\times2)$ surface to $c(4\times2)$ again by scanning the surface with $V_b=-1.2$ V.

The STM images were recorded using a constant current mode at 80 K with a tungsten tip. We can observe the surface structure without changing it using a sample bias voltage between -0.5 and +0.5 V. The STM images shown in this paper are recorded with $V_b=-0.4$ V. To inject carriers into the surface states, we temporarily fix the tip at the position of interest by cutting the feedback loop during image recording and change the bias voltage for 1 s while maintaining the

tip-surface distance. Here, we call this V_b change a bias pulse. Differential conductance images to measure the standing waves in the π^* band were recorded at 80 K using lock-in detection by modulating the bias voltage at 1.3 kHz.

The electronic states of the surface including the kink were studied by a first-principles calculation based on density-functional theory with a Ceperley-Alder-type exchange-correlation potential. We used an extended version of the program package TAPP.[22] The surface was simulated with a five atomic layer thick slab model with a six atomic layer thick vacuum region, and the bottom of the slab was terminated by virtual hydrogen atoms. The lateral periodicity of the slab was 7×4, as in the STM image simulation[23] and the unit cell contained two kinks. The Ge atoms were simulated with ultrasoft pseudopotentials. The wave function was expanded by a plane-wave basis set whose cutoff energy was 16 Ry. The number of the sampled k points in the first Brillouin zone was 4×4. By fixing the bottom layer, the rest of the atomic structure was optimized to make the maximum force acting on the structure less than 3×10^{-4} hartree a.u.$^{-1}$.

III. RESULTS AND DISCUSSION

A. Kink motions excited by carriers in surface states

The STM images in Fig. 2(a) show the motions of an *A*-type kink recorded after bias pulses to 0.8 V. In the figure, a small protrusion marked as **k** is a mobile kink and a round protrusion marked as **F** is accompanied with a kink fixed on its top. We used the fixed kink as a marker for the motion of the mobile kink. The fixed kink never moves by injecting electrons with a bias pulse to 0.8 V.

There are defects at which the threshold bias voltage for kink motion is larger than 0.6 V for electron injection. The impurity in the subsurface shown as **F** in Fig. 2(a) is one of them. It is imaged as a round protrusion with $V_b = -0.4$ V and as a round dent with $V_b = +1.2$ V when there is no kink on it. These features resemble STM images of a donor observed on the GaAs(110) surface.[24] We consider that the observed round protrusion with $V_b = -0.4$ V is a doped Sb atom in the subsurface. The kink on the donor **F** in Fig. 2(a) can be erased by scanning the surface with the STM tip at $V_b = -1.5$ V, for example.

We can move both types of kinks shown in Figs. 1(d) and 1(e) in the dimer-row direction by injecting electrons into the surface.[6] To measure kink motion, we used a surface with one mobile kink on the dimer row. Kinks are always created on a dimer row as a pair. In our studies, one of the created kinks was fixed at a defect on the surface such as a donor in the subsurface or was erased by moving it to the step edge.

The positions of the mobile kink are plotted in Figs. 2(b)–2(d) after each injection of electrons into the dimer row including the kink by a single bias pulse to 0.6, 0.7, and 0.8 V for 1 s. Multiple data runs are presented in these figures for a variety of initial distances between the tip and kink. Here, we fixed the tip with the condition that $V_b = -0.4$ V and $I_t = 1.0$ nA. The electrons were injected at the origin of the ordinate axis in the figure, and the abscissa indicates the number of injection pulses. The positive (nega-
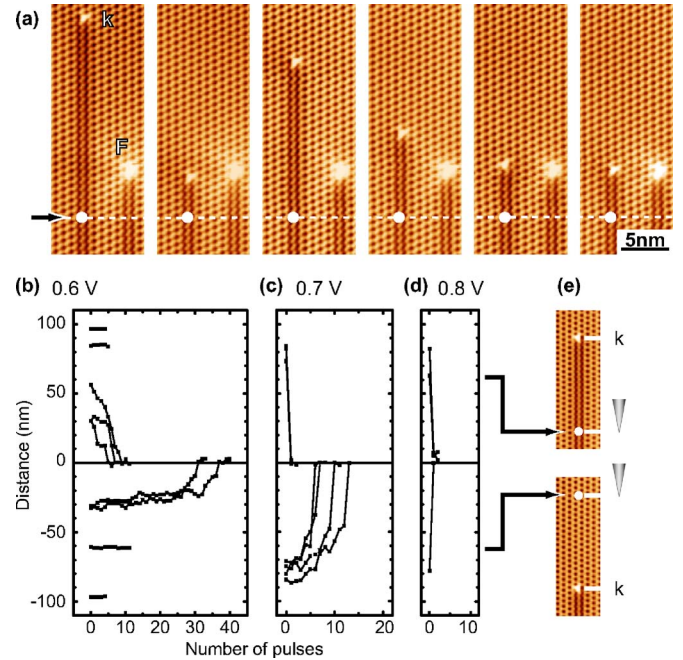

FIG. 2. (Color online) (a) STM images showing the motion of an *A*-type kink marked **k**. First, we observed the surface with the kink as in the left image with $V_b = -0.4$ V and $I_t = 1.0$ nA. Next, we injected current at a point indicated by the white circle and the solid arrow with a bias pulse to 0.8 V for 1 s. Then, we obtained the second left image. We repeated this procedure several times, and the images shown on the right side were obtained. A round protrusion **F** with a fixed kink is an impurity in the subsurface and was used as a marker for the motion of the mobile kink **k**. [(b)–(d)] Distance between the kink and the injection point in the dimer-row direction is plotted as a function of the number of bias pulses after each pulse from −0.4 V to (b) 0.6 V, (c) 0.7 V, and (d) 0.8 V for 1 s was applied at a point on the dimer row including the kink. The positive (negative) distance indicates that the electron was injected on the $p(2 \times 2)$ ($c(4 \times 2)$) area of the dimer row as schematically illustrated in (e).

tive) value of the kink position indicates that the current is injected into the $p(2 \times 2)$ ($c(4 \times 2)$) area of the dimer row including the kink, as schematically shown in Fig. 2(e). The tunneling current increased from 1.0 nA to 13, 17, and 25 nA for bias changes of 0.6, 0.7 and 0.8 V, respectively.

The kink generally moves toward the tunneling point after each bias pulse, but it sometimes moves in the opposite direction. This trend is not seen in Fig. 2(b) when the initial distance between the kink and the tunneling point is large. The kink moved back and forth when the distance was 85 nm for injection on the $p(2 \times 2)$ area and when it was 60 nm for injection on the $c(4 \times 2)$ area. The kink rarely moved when the distance was 98 nm for injection on both areas. The probability P of the kink motion per bias pulse for a fixed duration decreases with increasing distance between the kink and the injection point. Here, we define the critical distance d_c for kink motion as the distance for $P = 0.5$. It is 85 and 50 nm when current is injected into the $p(2 \times 2)$ and $c(4 \times 2)$ surfaces in Fig. 2(b), respectively, using a bias pulse of 0.6 V. The probability decreases to less than 10% when the distance is more than 100 nm. The value of d_c increases
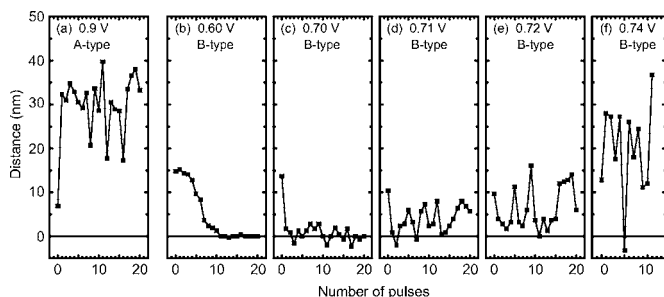
FIG. 3. (a) Distance between an *A*-type kink and the injection point in the dimer-row including the kink as a function of the number of bias pulses after each pulse from −0.4 to 0.9 V for 1 s was applied at the point. [(b)–(f)] Distance between a *B*-type kink and the injection point in the dimer-row including the kink as a function of the number of bias pulses after each pulse from −0.4 V to (b) 0.60 V, (c) 0.70 V, (d) 0.71 V, (e) 0.72 V, and (f) 0.74 V for 1 s was applied at the point. The center of the random motion is under the tip for 0.60 and 0.70 V, and the distance between the *B*-type kink and the injection point rapidly increases with increasing V_b during the pulse.

to more than 100 nm with increasing V_b during the pulse to over 0.7 V on the $p(2\times2)$ surface. It is, however, difficult to discuss the kink motions for such a long distance quantitatively because *P* is affected by inhomogeneously distributed defects near the surface. As in Fig. 2(a), for example, the kink on top of the subsurface donor is not mobile for a bias pulse less than 0.8 V. Even when the kink is not on a donor, *P* becomes small around the donor.

After a number of bias pulses, the kink comes close to the injection point and randomly moves in the dimer-row direction due to the pulse. The center position of the random motion is at the injection point for pulses of 0.6 and 0.7 V. The widths of the random motion are 1 and 3 nm for pulses of 0.6 and 0.7 V, respectively. The distance between the center position and the injection point increases with increasing V_b for pulses above 0.7 V.[6] The center positions are 8 and 30 nm from the injection point for pulses of 0.8 and 0.9 V, respectively. The result for 0.9 V is shown in Fig. 3(a). In these stationary states, the surface structure at the injection point is $p(2\times2)$.

Similar motions were observed for a *B*-type kink, as shown in Fig. 1(e). The kink position after each pulse for 1 s is plotted in Figs. 3(b)–3(f). It randomly moves in the dimer-row direction as seen for an *A*-type kink. The distance between the injection point and the center of the random kink motion increases more rapidly with increasing V_b during a pulse from 0.7 V than for an *A*-type kink. For example, it is more than 50 nm for a *B*-type kink using a pulse of 0.8 V, while it is 8 nm for an *A*-type kink.

Another type of kink can be formed at a "faulted" $c(4\times2)$ wire on the $p(2\times2)$ surface, as shown in Figs. 4(a)–4(c). It randomly moves due to a bias pulse, and the center of the motion is almost at the injection point when the V_b during a pulse is between 0.6 and 0.9 V, as shown in Figs. 4(d) and 4(e) for V_b=0.7 and 0.8 V. In contrast to *A*- and *B*-type kinks, the total length of the $c(4\times2)$ area is kept constant before and after the motion of this kink, as shown in Figs. 4(a) and 4(b).
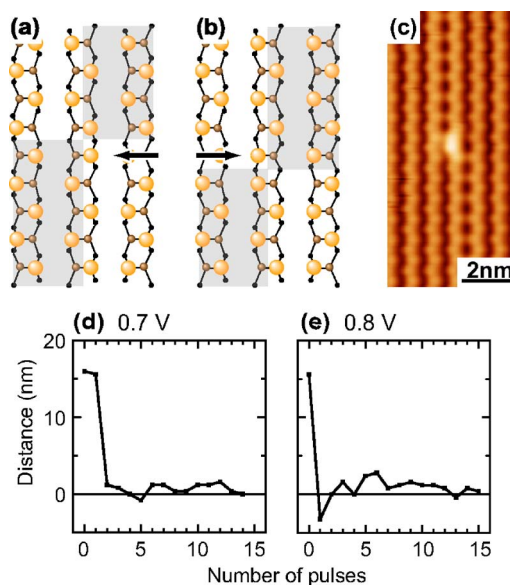

FIG. 4. (Color online) [(a) and (b)] Schematic models of a kink at a faulted $c(4\times2)$ wire on the $p(2\times2)$ surface. The arrow indicates the position of the kink. The position of the kink is different in these two figures. However, the total length of the $c(4\times2)$ area is the same before and after the kink motion in the dimer-row direction. (c) STM image of the kink at a faulted $c(4\times2)$ wire on the $p(2\times2)$ surface. [(d) and (e)] Distance between a faulted kink and the injection point in the dimer-row direction as a function of the number of bias pulses after each pulse from −0.4 V to (d) 0.7 V and (e) 0.8 V for 1 s was applied at the point on the dimer row including the kink. The kink moves to the electron injection point and then moves randomly around there.

These experimental results indicate that both the sample bias voltage and the local surface structure around the kink determine the most stable position for the kink motion. A buckled Ge dimer has an electric dipole, and the electric field due to the bias voltage between the substrate and the STM tip changes the energy of the dimer. Besides that, the lattice strain energy depends on the local structure. These two competing mechanisms determine the local atomic structure.[8] The subsurface donor, which affects kink motion, changes the local electric field and lattice distortion. We will discuss these effects further in Sec. III F.

Kink motion in the dimer-row direction can be excited also by injecting electrons into other dimer rows.[6] The critical distance for kink motion is much smaller in the dimer-axis direction than in the dimer-row direction for the same injection conditions as in Fig. 2(a); it is 6 nm for a 0.6 V pulse and 10 nm for a 0.7 V pulse on the $c(4\times2)$ surface, and 9 nm for a 0.6 V pulse and 27 nm for a 0.7 V pulse on the $p(2\times2)$ surface. On the $c(4\times2)$ surface, d_c in the dimer-axis direction is shorter than that on the $p(2\times2)$ surface for pulses of the same V_b. This trend is the same as for d_c in the dimer-row direction.

To further study how electron propagation in the dimer-axis direction depends on the superstructure, we prepared thin $c(4\times2)$ areas of different widths between a *B*-type kink and an injection point on the $p(2\times2)$ surface as in Figs. 5(a)–5(e). The probability of kink motion was measured as a
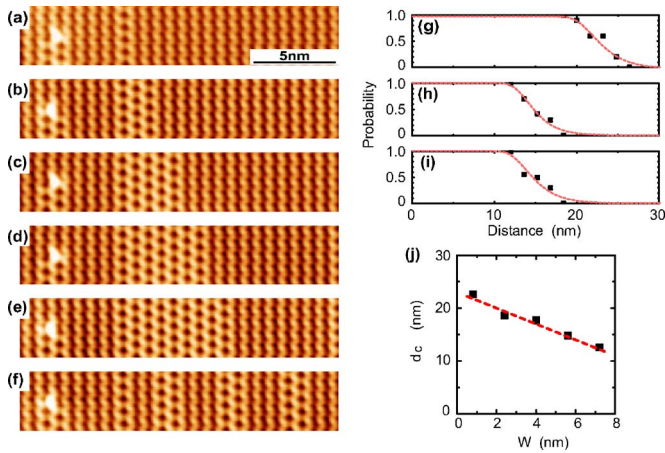
FIG. 5. (Color online) [(a)–(f)] STM images showing surfaces with a B-type kink and thin $c(4 \times 2)$ areas of different widths. The current was injected on the $p(2 \times 2)$ surface opposite to the $c(4 \times 2)$ area near the kink. [(g)–(i)] The probability of kink motion by a bias pulse to 0.7 V as a function of the distance between the kink and the tunneling point for the surfaces shown in (a), (d), and (f), respectively. (j) The values of d_c as a function of the total width W of the $c(4 \times 2)$ area. The dotted line indicates the linear relation $d_c = -1.5W + 23$ nm fitted to the experimental data.

function of the distance between the kink and the injection point using bias pulses to 0.7 V for 1 s. Some of the results are given in Figs. 5(g) and 5(h) for the surfaces shown in Figs. 5(a) and 5(d). The tip position was fixed with the condition $V_b = -0.4$ V and $I_t = 1.0$ nA. The critical distance decreases with the increasing width of the $c(4 \times 2)$ surface, W, between the kink and the injection point from 27 nm for the surface without any $c(4 \times 2)$ areas. Figure 5(j) shows the relation between d_c and W; d_c linearly depends on W.

No significant difference was observed in d_c on surfaces where the total width of the $c(4 \times 2)$ area was the same, e.g., Figs. 5(d) and 5(f). The probability of the kink motion is plotted in Fig. 5(i) for the surface shown in Fig. 5(f). On this surface, there are seven pairs of adjacent dimer rows, where the buckling orientation of the dimers in the dimer-axis direction is opposite to each other between the kink and the injection point. The number of dimer pairs is the same as that in Fig. 5(d). Here, we call this a "$c(4 \times 2)$ pair." The probability changes with distance on these surfaces are similar, as seen in Figs. 5(h) and 5(i). It is noted that the number of $c(4 \times 2)$ pairs between the kink and the electron injection point becomes 5 in Fig. 5(f) when the distance between them becomes less than d_c. However, this caused little effect on the probability within the statistical accuracy of the present experiment, although we can expect an increase of the probability for a distance shorter than d_c. More quantitative measurements of the probability are necessary to discuss how the split of the $c(4 \times 2)$ area affects electron propagation in the dimer direction.

In the case of hole injection, we used a bias pulse from -0.4 V to less than -0.7 V to create and move a kink on the $p(2 \times 2)$ surface. Figures 6(a)–6(d) show a $c(4 \times 2)$ area made by a pulse to -0.8 V and a random motion of a kink. Kink pairs are created on several dimer rows around the hole
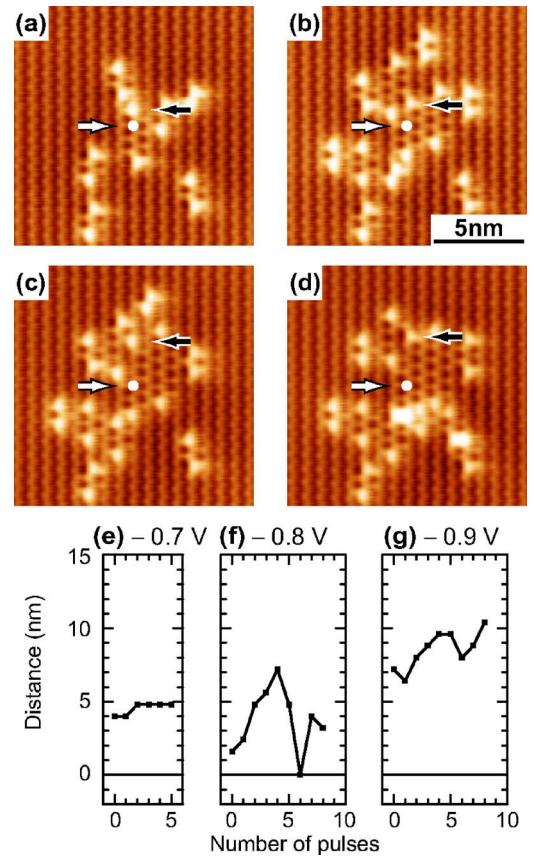

FIG. 6. (Color online) [(a)–(d)] STM images showing the $c(4 \times 2)$ areas around a hole injection point before and after three successive injections to $V_b = -0.8$ V. A white arrow and circle on each figure indicate the injection point, and a solid arrow indicates the kink on the dimer row including the injection point. [(e)–(g)] Distance between the injection point and the kink on the dimer row including the injection point as a function of the number of bias pulses from -0.4 V to (e) -0.7 V, (f) -0.8 V, and (g) -0.9 V for 1 s. The current during each pulse was (e) 7 nA, (f) 10 nA, and (g) 16 nA.

injection point, in contrast to the case of electron injection. The $c(4 \times 2)$ area increases by repeating the bias pulse and finally saturates.[5] The distance between the injection point and the kink on the dimer row including the injection point is plotted as a function of the number of bias pulses in Figs. 6(e)–6(g). The $c(4 \times 2)$ area saturated after a few pulses to $V_b = -0.7$ V and gradually increased after eight pulses to -0.9 V.

The critical distance d_c for an A-type kink increases with decreasing V_b for pulses below -0.7 V. The anisotropy of d_c between the dimer-axis direction and the dimer-row direction is smaller than that for kink motion by electron injection[6]; d_c in the dimer-row direction is almost twice as large as that in the dimer-axis direction. Consequently, the shape of the created $c(4 \times 2)$ area is two dimensional as in Figs. 6(a)–6(d). The kink never moves for V_b during the pulse between -0.6 and -0.4 V. In other words, the center of the random motion never comes back to the injection point with increasing V_b during the pulse in the case of hole injection. As for the B-type kink, quantitative study on its motion is difficult be-

cause a $c(4\times2)$ area is always created around the hole injection point on the $p(2\times2)$ surface caused by the bias pulse for the observation of its motion.

B. Superstructure transformation induced by carrier injection

The energy transfer from the tunneling carriers to the dimer induces the structure transformation shown in Fig. 1(c) through electron-lattice interaction during STM observation; kink pairs are formed[5] and successively move as in the previous section. For electron injection, the threshold bias voltage for transformation is 0.2 V higher than for kink movement. When the bias voltage is between 0.6 and 0.7 V, the center position of the random kink motion is just at the injection point. Consequently, even when a kink pair is formed near the STM tip on the dimer row by electronic excitation, successive electron injection induces pair annihilation, and the $p(2\times2)$ area between the two kinks changes to $c(4\times2)$. The kink formed by electron injection never comes back to the injection point with $V_b \geq 0.8$ V, and a stable $p(2\times2)$ structure is observed by scanning the surface with the same V_b. This determines the threshold bias voltage of the structure transformation by scanning the surface with the STM tip.

The $p(2\times2)$ structure is stabilized against the decrease of V_b from 0.8 V only when one of the two kinks, which were formed as a pair on the same dimer row, vanishes at a step edge or is fixed at a point defect on the surface. Otherwise, the two kinks come close to each other under the STM tip with decreasing V_b below 0.8 V, and the $p(2\times2)$ area disappears. In this case, no hysteresis is expected in the structure transformation from the $p(2\times2)$ to $c(4\times2)$ by changing V_b continuously. On the other hand, for hole injection, the threshold bias voltage of the structure transformation corresponds to that of kink formation and movement. Moreover, the $c(4\times2)$ area once formed remains even after increasing the bias voltage to a value between -0.5 and 0.5 V from that lower than -0.7 V because the kinks never come back to the injection point by this bias change.

C. Surface electronic states

The dangling-bond π^* state on the clean Ge(001)-$c(4\times2)$ has recently been clarified both experimentally and theoretically.[13] Experimentally, the bottom of the state is 0.3 eV above the bulk valence-band top at $\bar{\Gamma}$. This is consistent with the band structure calculated for the $c(4\times2)$ surface, as shown in Fig. 7(a). Here, the dispersion relations are plotted as functions of the wave number with the 2×1 symmetry shown in Fig. 7(c) for simplicity. On the other hand, the bulk band gap was estimated to be narrower in the calculation than the experimentally known value, as it often happens in the band calculation based on the density-functional method. The π^* band [thick curve in Fig. 7(a)] is a quasi-one-dimensional state and largely disperses in the dimer-row direction, while the dispersion is small in the dimer-axis direction. The band structure for the $p(2\times2)$ surface[25] is shown in Fig. 7(b). The dispersion of the π^* state in the dimer-axis direction is larger than that on the
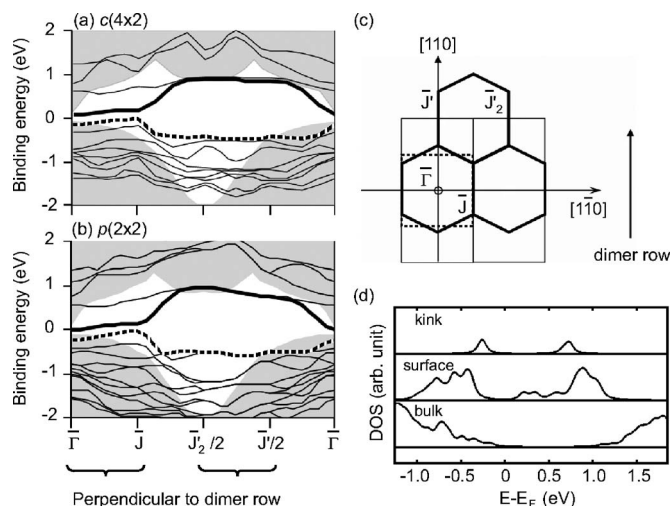

FIG. 7. [(a) and (b)] Surface electronic band structures around the Fermi energy (a) for the clean Ge(001) surface with the $c(4\times2)$ superstructure (Ref. 13) and (b) for the surface with the $p(2\times2)$ superstructure (Ref. 25). The axes are defined for the 2×1 surface as in (c). Gray areas are the bulk band projected to the surface. The thick curve in each figure indicates the π^* band. (c) The surface Brillouin zones for the $c(4\times2)$ (thick lines), (2×1) (thin lines), and $p(2\times2)$ (dotted line) surfaces. (d) Density of states for the kink, the surface, and the bulk obtained by first-principles calculations.

$c(4\times2)$ surface. On the other hand, little difference is seen for the dispersion in the dimer-row direction.

The structure of the dangling-bond valence π states is not so simple as that of the conduction band [the thick dotted curve in Figs. 7(a) and 7(b)]: the anisotropy of their dispersion is smaller than that of the π^* state, the energy of the bands is not maximum at the $\bar{\Gamma}$ point, and the surface state is in resonance to the bulk bands around $\bar{\Gamma}$ as in Fig. 7(a). Recent results of ARUPS on this surface[13] confirmed that the top of the valence band is the bulk state. Thus, the hole injected into the surface state from the STM tip propagates quasi-two-dimensionally in the surface hole bands and has a shorter lifetime than that of the electron in the π^* band because of scattering to the bulk states. The valence electronic states of the $p(2\times2)$ surface have no significant differences from those on the $c(4\times2)$ surface between E_F and -2.0 eV.

Figure 7(d) shows the calculated density of electronic states for the kink, the surface, and the bulk. We classified the states into these three categories by investigating the local electronic states. We used a width of 50 meV for each state to obtain this figure. The empty kink state is in the middle of the empty dangling-bond π^* state, while the filled kink state is higher than the top of the filled dangling-bond π state and a resonance in the bulk filled states. These well explain the bias-dependent image contrast of the kink in the STM observations.[23] The relation among the surface states and the bulk states is consistent with the above band calculation, although the bulk band gap and the absolute energy of the states are different from the observations.

D. Carrier propagation and energy relaxation
in the surface states

The electrons tunnel from the STM tip exclusively into the π^* surface states when the bias voltage is between 0.3 and 0.8 V. Even when the energy of the tunneling electron is larger than the bulk band-gap energy, the electrons are mainly injected into the surface states. The electron thus injected propagates in the π^* band and is inelastically scattered to the state with a lower energy in the same band or to other states. The kink is a scatterer for the electrons in the surface states. Actually, a standing wave of the π^* state electron is observed on both sides of the kink by the scattering. The π^* electron can go into the kink state when its energy is larger than the bottom of the empty kink state [see Fig. 7(d)]. Then, part of such electrons in the kink state induces the kink motion through electron-lattice interaction.[7] This indicates that we can detect the propagation of the carriers from the injection point to the kink position by observing the kink motion.

The observed anisotropy of d_c for electron injection is attributed to the anisotropic propagation of the electron wave packet in the π^* state. The dispersion of the π^* band in the dimer-row direction is much larger than that in the dimer-axis direction as in the band calculation shown in Fig. 7(a) and 7(b).

On the $p(2\times2)$ surface, d_c in both the dimer-axis and dimer-row directions is larger than that on the $c(4\times2)$ surface as in Figs. 2 and 5. The different behaviors in the dimer-axis direction can be explained by the dispersion relation of the π^* band in this direction. The longer d_c in the dimer-axis direction is consistent with the larger dispersion on $p(2\times2)$ as in Figs. 7(a) and 7(b), that is, the larger electron transfer between the neighboring dimer rows in this band. On the contrary, there is no significant difference of the π^* band dispersion in the dimer-row direction in Figs. 7(a) and 7(b). Furthermore, according to previous results on the standing-wave observation of the π^* state electrons,[26] the dispersion on the $c(4\times2)$ surface is larger than that on the $p(2\times2)$ surface. Thus, the above explanation is not applicable to the experimental result in this direction.

Another possible origin for the difference of d_c is the energy relaxation of the π^* electrons. They lose their energy during propagation in the π^* band through electron-phonon and electron-electron interactions. These inelastic scattering processes can determine the critical distance. To discuss the energy relaxation on both surfaces, we measured the decay behavior of the π^* electron standing waves from a single step on the surface. It is known that the decay behaviors at low temperature is mainly attributed to the decoherence of the electron wave at the surface and is characterized by a phase coherence length L_ϕ.[27] Inelastic scattering processes destroy the coherence of the surface-state electron.

We obtained differential conductance (dI/dV) images with standing waves on the lower terrace of the single step. For the comparison between $c(4\times2)$ and $p(2\times2)$, we simultaneously observed a surface with both superstructures so that any artifacts depending on the electronic states of the STM tip and the bias modulation for the lock-in detection affected the image of both structures in the same way. The
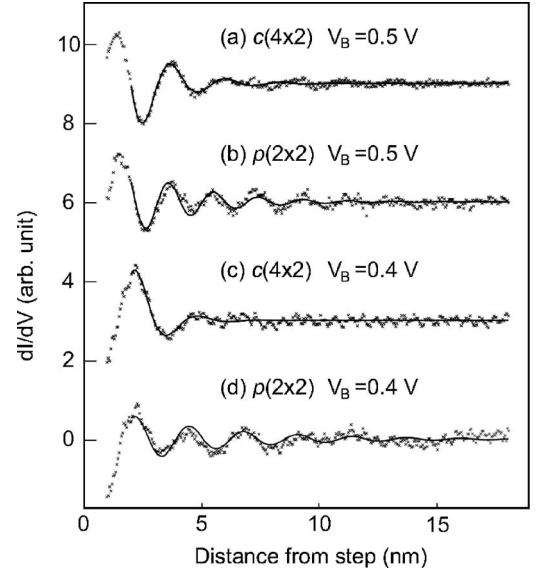

FIG. 8. Cross sections of the differential conductance (dI/dV) images ($\times$) in the dimer row direction, showing π^* electron standing waves on the lower terrace of a single step. The origin of the horizontal axis is the step edge. The sample bias was [(a) and (b)] 0.5 V or [(c) and (d)] 0.4 V. The surface structure was [(a) and (c)] $c(4\times2)$ or [(b) and (d)] $p(2\times2)$. Each solid curve denotes Eq. (1) with the parameters fitted to each standing wave.

cross sections of the differential conductance image from the step are plotted in Figs. 8(a)–8(d) for $V_b=0.4$ and 0.5 V on both $c(4\times2)$ and $p(2\times2)$. We fitted each wave to the equation

$$dI/dV = A \exp(-2x/L)\sin(2kx + \delta).\qquad(1)$$

Here, we assume that the formula for a one-dimensional electron system is applicable to the π^* electron and introduce L, the decay length of the wave, similar to the two-dimensional electron system.[27] In Eq. (1), A and δ are the amplitude and the phase shift of the standing wave, respectively, and k is the wave number of the π^* electron. In the fitting, we neglected data close to the step edge (<2 nm) to avoid any wave distortion caused by the presence of the step edge.[26] The fitted values of the parameters are given in Table I. On the $p(2\times2)$ surface, L is longer for both bias voltages than on the $c(4\times2)$ surface. The observed decay length is not always L_ϕ because it includes other sources of decay such as thermal broadening of the Fermi-Dirac distribution at

TABLE I. Values of the parameters for the fitting of the standing waves.

Structure	V_b (V)	k (nm^{-1})	L (nm)
$c(4\times2)$	0.5	1.4	3.0
$p(2\times2)$	0.5	1.7	5.4
$c(4\times2)$	0.4	1.2	2.0
$p(2\times2)$	0.4	1.4	8.0

the STM tip and bias modulation for the lock-in detection of the dI/dV image.

For discussion of the fitted values of L, we first estimate the contributions of thermal broadening and the bias modulation to it. In both cases, the decay lengths due to them are proportional to the derivative of the dispersion relation $dE/dk = \hbar^2 k/m$. The values are $1/2$ eV nm for $c(4 \times 2)$ and $1/3$ eV nm for $p(2 \times 2)$ when we use the observed relation between wave number and electron energy in Table I. According to Ref. 27 the decay length due to the thermal broadening, L_T, is given as $2.7(dE/dk)/2\pi k_B T$. Then, $L_T \approx 30$ nm for $c(4 \times 2)$ and ≈ 20 nm for $p(2 \times 2)$ at 80 K. For lock-in detection, the bias modulation ΔV was 20 mV peak to peak. This gives[27] the decay length $L_M \approx (dE/dk)/e\Delta V \approx 25$ nm for $c(4 \times 2)$ and ≈ 17 nm for $p(2 \times 2)$. All these values are longer than the observed decay lengths. Moreover, opposite to the observation, the calculated decay lengths for $c(4 \times 2)$ are longer than those for $p(2 \times 2)$ because of the difference of dE/dk. This indicates that these two mechanisms are not the main origins of the observed decay of the standing wave.

In the present measurement, thus, we can conclude that the main difference between the observed decay lengths is attributed to L_ϕ, the phase coherence length due to inelastic scattering of the π^* state electrons. It is longer on the $p(2 \times 2)$ surface. The energy relaxation of the π^* electrons can explain the result that d_c in both the dimer-row and dimer-axis directions on this surface is longer than that on the $p(2 \times 2)$ surface. The difference between the electron-phonon scattering rates may explain that of the phase coherence lengths. The interaction between the surface-state electron and the surface phonon depends on the superstructure.

In the case of hole injection, the anisotropy of d_c is small. This is consistent with the small anisotropy of the π state bands, as shown in Figs. 7(a) and 7(b). A hole in the π state must have a shorter lifetime than the π^* electron because the π state is a resonance to the bulk states. The energy in the surface states rapidly moves to the bulk states.

E. Electron-scattering model for the critical distance

The linear relation between d_c and W in Fig. 5(j) can be reproduced by adopting a simple model with inelastic electron scattering from the π^* state. Here, we make the following two assumptions. The first is that the π^* electron transfer in the dimer-row direction is much larger than that in the dimer-axis direction. Then, once the electron is transferred into a dimer row, the electron homogeneously occupies the dimer row before being transferred to the neighboring dimer row. This assumption is based on the experimental result that the critical distance is determined only by the distance in the dimer-axis direction between the dimer row including the kink and that with the carrier-injection point, provided that the distance in the dimer-row direction is less than 40 nm.[6] The second assumption is that an electron transferred into a dimer row inelastically loses its energy to less than the threshold of kink motion with a certain probability q before being transferred into the next dimer row toward the kink. The probability depends on the surface structure, and here

we define q for $c(4 \times 2)$ and $p(2 \times 2)$ as $q_{c(4 \times 2)}$ and $q_{p(2 \times 2)}$, respectively.

Now, we consider a $p(2 \times 2)$ surface with a $c(4 \times 2)$ area between the kink and the injection point as in Fig. 5. Here, we define $m_{p(2 \times 2)}$ ($m_{c(4 \times 2)}$) as the number of the dimer row where the buckling orientation of the dimers is the same as (opposite to) that in the neighboring dimer row on the kink side. This indicates the $p(2 \times 2)$ ($c(4 \times 2)$) structure. Then, the total number of dimer rows between the kink and the injection point is $m_{c(4 \times 2)} + m_{p(2 \times 2)}$.

When we further assume that each motion of the electron between the dimer rows is independent, the probability $P(m_{c(4 \times 2)}, m_{p(2 \times 2)})$ that at least one electron moves the kink through ($m_{c(4 \times 2)} + m_{p(2 \times 2)}$) dimer rows after injecting N electrons at the injection point is given as

$$P(m_{c(4 \times 2)}, m_{p(2 \times 2)}) = 1 - \big[1 - s(1 - q_{c(4 \times 2)})^{m_{c(4 \times 2)}}$$
$$\times (1 - q_{p(2 \times 2)})^{m_{p(2 \times 2)}}\big]^N. \quad (2)$$

Here, s is the probability that a single electron in the dimer row including the kink moves it. This equation well reproduces the experimental results with appropriate parameters as the dotted curves in Figs. 5(g) and 5(h).

To show the linear relation between d_c and W, we define $m_c \equiv m_{c(4 \times 2)}$ and $m_p \equiv m_{p(2 \times 2)}$ at d_c, that is, $P(m_c, m_p) = 0.5$, $d_c = a(m_c + m_p)$, $W = am_c$, and a is the period of the dimer row. Then, $P(m_c, m_p) = 0.5$ can be written as

$$m_c \log(1 - q_{c(4 \times 2)}) + m_p \log(1 - q_{p(2 \times 2)})$$
$$= -\log(s) + \log(1 - 0.5^{1/N}). \quad (3)$$

When we define m_{c0} and m_{p0} using the equations $P(m_{c0}, 0) = 0.5$ and $P(0, m_{p0}) = 0.5$, we obtain

$$m_{c0} \log(1 - q_{c(4 \times 2)}) = -\log(s) + \log(1 - 0.5^{1/N}) \quad (4)$$

and

$$m_{p0} \log(1 - q_{p(2 \times 2)}) = -\log(s) + \log(1 - 0.5^{1/N}). \quad (5)$$

From these equations, Eq. (3) can be rewritten as $m_c/m_{c0} + m_p/m_{p0} = 1$.

In the experiments, m_{c0} and m_{p0} are determined on the pure $c(4 \times 2)$ and $p(2 \times 2)$ surfaces. The linear relation can be written as $d_c = -(m_{p0} - m_{c0})W/m_{c0} + am_{p0}$. Using the observed values $am_{c0} = 10.4$ nm and $am_{p0} = 27$ nm,[6] we obtain $d_c = -1.6W + 27$ nm. The coefficient of the linear term agrees with the slope of the dashed line in Fig. 5(j), while the constant term is higher than the experimental value.

F. Direction of kink motion by electron injection

The distance between the current injection point and the center of the random walk of a kink in the dimer-row direction increases with increasing the positive bias voltage during the injection pulse. These features resemble one-dimensional motions of a particle in a washboard plus a long-range attractive potential. Under the tip apex is the point of the potential minimum for the pulses to 0.6 and 0.7 V. When V_b during the pulse is further increased, the

minimum point shifts so as to make the superstructure at the injection point $p(2\times2)$. We will discuss the origin of this attractive potential.

The electric field induced by the STM tip is the first we should consider as the origin of the potential.[9] Because of the electric dipole at the Ge dimers, the surface energy should depend on the external electric field; the upper (lower) Ge atom of the dimer is negatively (positively) charged. The positive sample bias qualitatively favors the $p(2\times2)$ structure to reduce the dipole energy among the dimers. This is consistent with the observed shift of the center position for the random kink motion.

On the basis of this scenario, the change of the surface energy due to the electric field was calculated using first-principles calculations in a homogeneous electric field for both Ge(001) and Si(001). First, it was reported[28] that the $p(2\times2)$ structure can be the ground state for Si(001) for positive V_b. In a later calculation,[29] however, the $c(4\times2)$ structure is still the ground state of both surfaces for positive V_b. In these calculations, the electric field is simply introduced between the semiconductor slabs. For a quantitative discussion, however, a more realistic calculation, such as the effective screening medium method,[30] is necessary by including the charge redistribution in both the semiconductor and the metal STM tip.

The stable point of the kink at a faulted $c(4\times2)$ wire on the $p(4\times2)$ surface shown in Fig. 4(c) is under the tip when the bias voltage is positive and at least less than 0.9 V. In this case, the sum of the dipole energy is independent of the kink position under a homogeneous electric field because the total length of the $c(4\times2)$ wire is the same after kink motion, as illustrated in Figs. 4(a) and 4(b). This result indicates that the kink itself is the most stable under the tip irrespective of the strength of the electric field in this range. As indicated in Fig. 7(d), the empty state of the kink is higher than the bottom of the dimer π^* band. Consequently, a kink is less negatively charged than the other dimers. Under a positive sample bias, this stabilizes the kink under the tip as observed. For a detailed discussion of kink motion, however, we have to consider the charge dynamics in the excited states as well as its distribution more quantitatively.

Another possible origin of the potential for kink motion is the long-range attractive atomic force between the STM tip and the surface.[31] This expands the Ge lattice near the surface toward the tip. The lattice strain energy under the

Ge dimers is smaller in the $p(2\times2)$ structure than in the $c(4\times2)$ structure.[8] The attractive force must change the energy difference of the lattice strain under the STM tip. Again, for the quantitative discussion, we need a microscopic calculation on the relation between the deformation and the stability of the superstructure.

IV. CONCLUSION

We have demonstrated that carriers injected into surface states induce a one-dimensional motion of a kink on the Ge(001) clean surface. The critical distance of the motion between the injection points and the kink was measured and used for the discussion on the propagation of the carriers in the surface states. It depends on the local superstructure, whether it is $c(4\times2)$ or $p(2\times2)$. The anisotropy of the distance and its dependence on the local superstructure are consistent with the electronic states studied by ARUPS, standing-wave observations, and band calculations. The critical distance is determined by electronic energy transfer between the dimers through propagation of the injected carriers and its energy relaxation. We also found that the stable position of a kink depends on the sample bias voltage during carrier injection. This suggests that the electric field due to the STM tip fixes the direction of kink motion through the electric dipole of the Ge dimers on the surface.

The formation and the motion of a kink on the surface by injected carriers well explain the local transformation of its superstructures. The same mechanism is applicable for structural changes on the clean Si(001) surface under STM observations.[17–20] Moreover, application of this mechanism is not limited to atoms on clean surfaces. It was previously proposed that carrier injection into a halogen-adsorbed Si(001) surface from an STM tip induces motion of the adsorbed atoms.[32]

*Present address: RIKEN/SPring-8, 1-1-1 Kouto, Sayo-cho, Sayo, Hyogo 679-5148, Japan. Electronic address: y-takagi@spring8.or.jp

†Electronic address: komori@issp.u-tokyo.ac.jp

[1] T. C. Shen, C. Wang, G. Abeln, J. R. Tucker, J. W. Lyding, Ph. Avouris, and R. Walkup, Science **268**, 1590 (1995).

[2] B. C. Stipe, M. A. Rezaei, W. Ho, S. Gao, M. Persson, and B. I. Lundqvist, Phys. Rev. Lett. **78**, 4410 (1997).

[3] B. C. Stipe, M. A. Rezaei, and W. Ho, Science **279**, 1907 (1997).

[4] H. Ueba, Surf. Rev. Lett. **10**, 771 (2003).

[5] Y. Takagi, Y. Yoshimoto, K. Nakatsuji, and F. Komori, Surf. Sci. **559**, 1 (2004).

[6] Y. Takagi, Y. Yoshimoto, K. Nakatsuji, and F. Komori, J. Phys. Soc. Jpn. **74**, 3143 (2005).

[7] H. Kawai and O. Narikiyo, J. Phys. Soc. Jpn. **73**, 2362 (2004).

[8] Y. Yoshimoto, Y. Nakamura, H. Kawai, M. Tsukada, and M. Nakayama, Phys. Rev. B **61**, 1965 (2000).

[9] Y. Takagi, Y. Yoshimoto, K. Nakatsuji, and F. Komori, J. Phys. Soc. Jpn. **72**, 2425 (2003).

[10] S. D. Kevan, Phys. Rev. B **32**, 2344 (1985).

[11] E. Landemark, C. J. Karlsson, L. S. O Johansson, and R. I. G. Uhrberg, Phys. Rev. B **49**, 16523 (1994).

[12] L. Kipp, R. Manzke, and M. Skibowski, Solid State Commun. **B93**, 603 (1995).

[13] K. Nakatsuji, Y. Takagi, F. Komori, H. Kusuhara, and A. Ishii, Phys. Rev. B **72**, 241308(R) (2005).

[14] T. Uda, H. Shigekawa, Y. Sugawara, S. Mizuno, H. Tochihara, Y. Yamashita, J. Yoshinobu, K. Nakatsuji, H. Kawai, and F. Komori, Prog. Surf. Sci. **76**, 147 (2004).

[15] Y. Kondo, T. Amakusa, M. Iwatsuki, and H. Tokumoto, Surf. Sci. **453**, L318 (2000).

[16] T. Yokoyama and K. Takayanagi, Phys. Rev. B **61**, R5078 (2000).

[17] Y. Pennec, M. Horn von Hoegen, Xiaobin Zhu, D. C. Fortin, and M. R. Freeman, Phys. Rev. Lett. **96**, 026102 (2006).

[18] K. Sagisaka, D. Fujita, and G. Kido, Phys. Rev. Lett. **91**, 146103 (2003).

[19] D. Riedel, M. Lastapis, M. Martin, and G. Dujardin, Phys. Rev. B **69**, 121301(R) (2004).

[20] K. Sagisaka and D. Fujita, Phys. Rev. B **71**, 245319 (2005).

[21] Y. Naitoh, K. Nakatsuji, and F. Komori, J. Chem. Phys. **117**, 2832 (2002).

[22] J. Yamauchi, M. Tsukada, S. Watanabe, and O. Sugino, Phys. Rev. B **54**, 5586 (1996).

[23] Y. Takagi, Y. Yoshimoto, K. Nakatsuji, and F. Komori, Surf. Sci. **593**, 133 (2005).

[24] R. M. Feenstra, J. M. Woodall, and G. D. Pettit, Phys. Rev. Lett. **71**, 1176 (1993).

[25] A. Ishii and H. Kusuhara (private communication).

[26] K. Sagisaka and D. Fujita, Phys. Rev. B **72**, 235327 (2005).

[27] L. Bürgi, H. Brune, O. Jeandupeux, and K. Kern, J. Electron Spectrosc. Relat. Phenom. **109**, 33 (2000).

[28] K. Seino, W. G. Schmidt, and F. Bechstedt, Phys. Rev. Lett. **93**, 036101 (2004).

[29] J. Nakamura and A. Natori, Phys. Rev. B **71**, 113303 (2005).

[30] M. Otani and O. Sugino, Phys. Rev. B **73**, 115407 (2006).

[31] H. Hölscher, U. D. Schwarz, and R. Wiesendanger, Appl. Surf. Sci. **140**, 344 (1999).

[32] Y. Nakamura, Y. Mera, and K. Maeda, Surf. Sci. **531**, 68 (2003).